Ni-Mo Nanorod Bundles Grown within Nickel Foam for Excellent Electrochemical Performance

Jie Yuan[1], Hui Zhao[1], Ruizhuo Ouyang[*], Yuqing Miao[*]

Bismuth Science Research Institute, University of Shanghai for Science and Technology, Shanghai 200093, P. R. China
[*]E-mail: ouyangrz@usst.edu.cn (R. Ouyang); yqmiao@usst.edu.cn (Y. Miao).
[1]J. Yu and H. Zhao contributed equally to this work and should be considered as joint first authors

In this work, nanorod bundles of Ni-Mo-O were synthesized within nickel foam (NF) using a conventional hydrothermal method, which was the further vulcanized to form Ni-Mo-S upon doping sulfur. The NF/Ni-Mo-O and NF/Ni-Mo-S materials were characterized in terms of their morphology, composition and electrochemical properties. NF/Ni-Mo-O showed excellent performance as a supercapacitor. In addition, NF/Ni-Mo-S catalyzed the electrochemical oxidation of glucose in alkaline medium, exhibiting its potential application as a new fuel cell. Their excellent electrochemical performances greatly benefited from the preferred activity of NF/Ni-Mo-O and NF/Ni-Mo-S, efficient electron transfer over the electrode and high conductivity of NF.

1. INTRODUCTION

A lot of attention has been paid to the development of fuel cells. Glucose used as a fuel is advantageous because it is non-toxic, odorless and clean, unlike methanol and other biomass fuels [1-2]. Meanwhile, the huge amount of energy (2.87×10^3 kJ·mol^{-1}) preferred for fuel cell applications can be produced during the complete oxidation of glucose. Therefore, glucose can be regarded as a promising alternative fuel used to generate energy by directly converting chemical energy into electrical energy [3-4]. The catalytic oxidation of glucose is not only the key to developing glucose-based fuel cells, but has also been extensively used to analyze glucose in many fields such as food, medicine and biotechnology [4-7]. Recently, with the development of catalyst preparation technologies, inexpensive transition metal-based nanomaterials have proven to be potential catalyst candidates for glucose oxidation [8-11]. Due to their low cost and promising electrocatalytic properties, Ni/Mo-based nanomaterials have been considered as attractive alternatives to non-precious metals in fuel cells. Generally, the Mo doping promotes the electrochemical performance of Ni-based catalysts toward the oxidation of small molecules. In addition, various sulfides of non-precious metals have emerged as promising catalysts for

the electrochemical oxidation of glucose, including NiS_x [12-13], CoS_x [14] and MoS_2 [15], which indicates that S doping can increase the electron transfer, reduce the activation energy and improve the catalytic efficiency.

Herein, Ni-Mo-O nanorod bundles were synthesized *in-situ* within nickel foam (NF) to fabricate pseudocapacitors and Ni-Mo-S to catalyze the electrochemical oxidation of glucose. Such nanocatalysts are expected to form on the surface of NF leading to a three-dimensional structure with high specific surface area, excellent stability and enhanced electrocatalytic performance [16-17]. The electrochemical performance of both NF/Ni-Mo-O and NF/Ni-Mo-S was studied in detail.

2. EXPERIMENTS

2.1. Chemicals

$Ni(NO_3)_2 \cdot 6H_2O$, $(NH_4)_6Mo_7O_{24} \cdot 4H_2O$ and Na_2SO_3 were purchased from Aladdin Biotechnology Co., Ltd. (Shanghai, China). Nickel foam (thickness 1.5 mm, PPI 110, density $250 g/m^2$, porosity 98％) was form Suzhou Jia Shi De metal foam Co., Ltd (Suzhou, China). Solutions used in all experiments wereprepared with the deionized water.

2.2. In site growth of Ni-Mo-O nanorod bundles within nickel foam

Firstly, nickel foam (10 mm× 10 mm× 1 mm) was ultrasonically in alcohol, 1 M HCl solution and deionized water regularly for 20 min step by step, and dried by hot air for subsequent use.

Typically, 10 mL of 80 mM $Ni(NO_3)_2$ were mixed with 10 mL of 10 mM $(NH_4)_6Mo_7O_{24}$□ which was then vigorously stirred for an hour. Afterwards, the mixed solution and a piece of nickel foam were poured together into the stainless steel reaction kettle. The kettle was sealed and subsequently heated to 150 °C for 6 h in an oven. The nickel foam with Ni-Mo-O nanorod bundles growing outside was washed with deionized water for removing remaining reactants after cooling down to room temperature naturally. Finally, the NF/Ni-Mo-O nanocomposites were obtained after being dried at 50 °C under vacuum for 6 h. Similarly, Ni-Mo-O nanorod bundles were prepared in the same procedures without nickel foam.

2.3. Preparation of the NF/Ni-Mo-S composite

50 mg sodium sulfite (Na_2SO_3) was placed in the corundum crucible with the NF/Ni-Mo-O. The temperature of the tube furnace was raised from 25 °C to 500 °C and held at 500 °C for 2 h to obtain NF/Ni-Mo-S. In contrast, the NF/Ni-Mo-O was calcined without Na_2SO_3 at 500 °C to obtain the NF/Ni-Mo-O'.

2.4. Nanomaterial characterization

The morphologies of both NF/Ni-Mo-O and NF/Ni-Mo-S were observed by scanning electron microscopy (SEM; Hitachi S-4800). The transmission electron microscope (TEM) images was taken with A JEM-2100 microscope. The local elemental composition on the surface of samples were identified by the energy dispersive X-ray spectrometer (EDS; Thermo Fisher). The characterization of X-ray photoelectron spectroscopy (XPS; PerkinElmer) was carried out on a RBD upgraded PHI-5000C ESCA system. All electrochemical measurements were performed with a CHI 660D electrochemical workstation (CH Instruments) controlled by computer and software. A three-electrode system was employed by using the NF/Ni-Mo-O or NF/Ni-Mo-S mofidied electrode as the working electrode, on the other hand, the reference electrode used the saturated calomel electrode (SCE) and the counter electrode chose the platinum wire.

3. RESULTS AND DISCUSSION
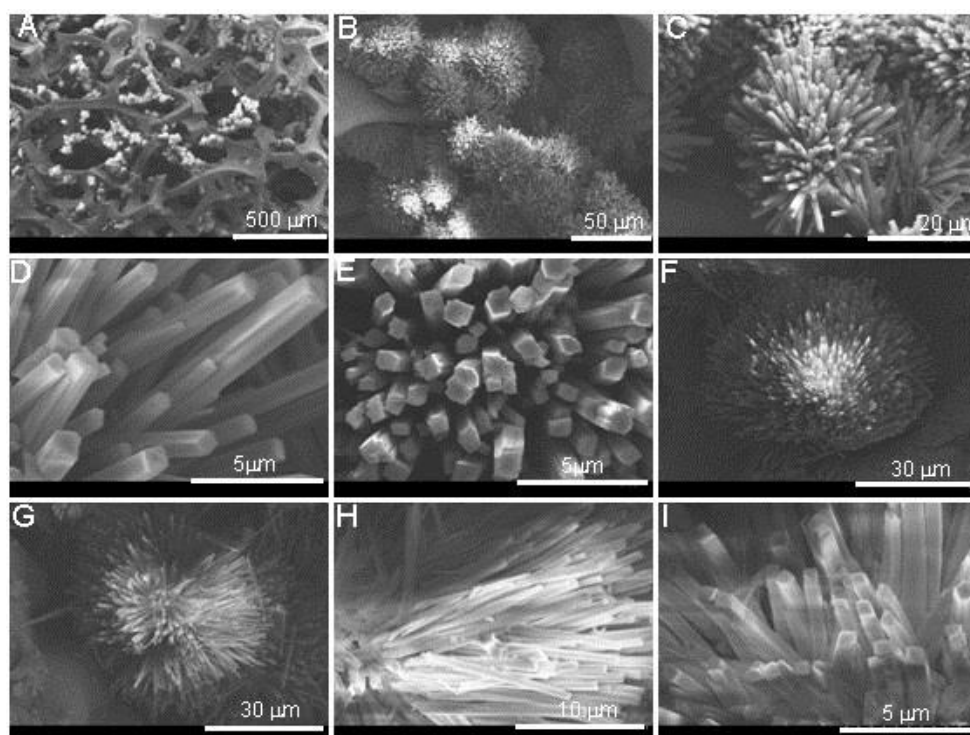
Figure 1. The morphologies of NF/Ni-Mo-O (A-E) and NF/Ni-Mo-S (F-I) observed using SEM.

Ni-Mo-O nanorod bundles were synthesized within NF using a conventional hydrothermal method. Fig. 1A shows the Ni-Mo-O nanorod bundles were uniformly grown and deposited on the surface of the porous NF support. The 3D structure of NF was uniformly covered by the Ni-Mo-O nanorod bundles, exhibiting a high specific surface area for the desired electrocatalytic reaction. The scanning electron microscopy (SEM) images in Fig. 1B-C show the uniform sphere-like nanorod bundles compacted on the surface and in the gaps of the NF support due to the formation of Ni-Mo-O nuclei. The high-magnified SEM images shown in Fig. 1D and E indicate that the spherical structure was

composed of numerous uniform polygon nanorods, which serve as building units that are scattered around from a common center [18]. Moreover, Ni-Mo-O nanorod bundles with a relatively uniform size of ~200 nm in diameter and lengths in the range of 400–600 nm were observed in the magnified SEM and the surface was fairly smooth with very few impurities observed, which is similar to that previously reported [19]. The morphology of NF/Ni-Mo-S is shown in Fig. 1F-I. No obvious differences were observed when compared to NF/Ni-Mo-O. This means that the high temperature calcination step (500 °C) and S doping did not affect the morphology.

The morphology of NF/Ni-Mo-O and NF/Ni-Mo-S was further characterized using transition electron microscopy (TEM) (Fig. 2A and B). The nanorod shape with an orderly compacted structure was observed for both materials. At the same time, no agglomeration was observed, which indicated the good dispersion of NF/Ni-Mo-O and NF/Ni-Mo-S. Furthermore, their shape did not significantly change after undergoing the reaction. Energy dispersive X-ray spectroscopy (EDS) was used to analyze the distribution and elemental composition of NF/Ni-Mo-O and NF/Ni-Mo-S. Fig. 2C shows the presence of Ni, Mo and O in NF/Ni-Mo-O. Similarly, Fig. 2D verified the successful doping of S in NF/Ni-Mo-S. The presence of O may originate from residual water molecules and oxidized NF/Ni-Mo-O. It was worth noting that the atomic ratio of O to S accounted was low in NF/Ni-Mo-O and NF/Ni-Mo-S.
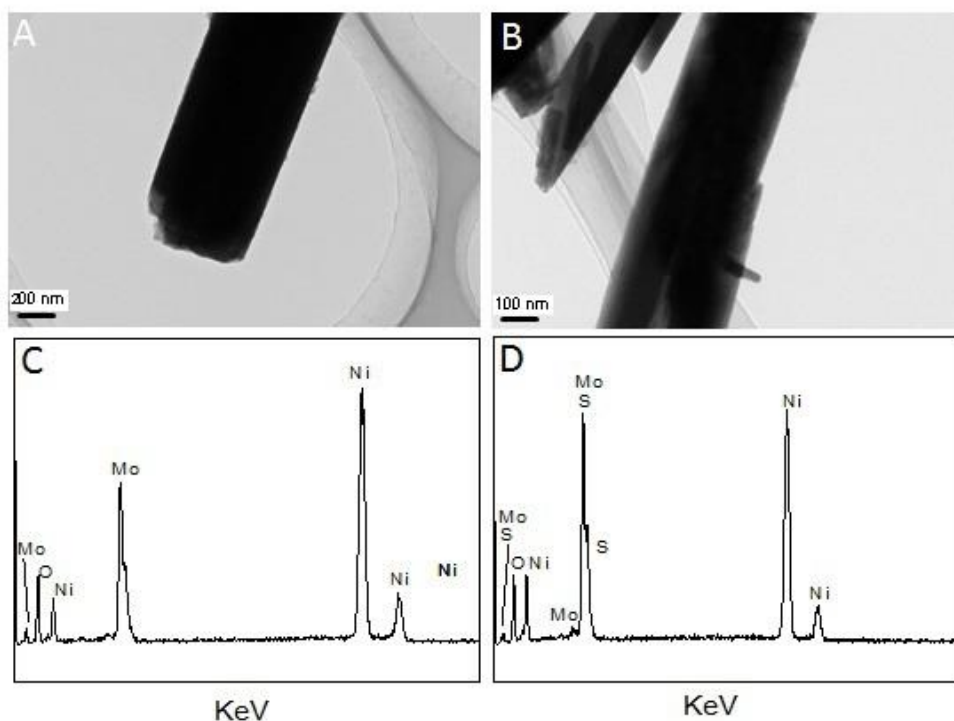
Figure 2. TEM images obtained for (A) NF/Ni-Mo-O and (B)NF/Ni-Mo-S. EDS analysis of (C) NF/Ni-Mo-O and (D) NF/Ni-Mo-S.

The composition, distribution and chemical state of the elements in NF/Ni-Mo-S were investigated using XPS (Fig. 3). The fitted XPS spectra of Ni, Mo and O imply the presence of Ni, Mo , O and S. Fig. 3A shows the fitted Ni 2p spectrum; two double peaks observed at 873.5/880.1 eV and

855.8/861.7 eV were assigned to Ni^{II} 2p$_{1/2}$ and Ni^{II} 2p$_{3/2}$, respectively. The peak observed at 857.8 eV was attributed to Ni^0 2p$_{3/2}$ satellite [20]. In addition, the satellite peak reflects the elemental state in Ni-Mo [21]. In Fig. 3B, the peaks observed at 232.3, 233.2 and 235.5 eV correspond to molybdenum trioxide and nickel molybdate (Mo 3d$_{5/2}$), molybdenum disulfide and nickel molybdate (Mo 3d$_{3/2}$), and MoO$_x$ (Mo 3d$_{3/2}$), respectively [22-23]. The O 1s peak located at 530.5 eV was ascribed to the binding of O to Mo (MoO$_x$) and Ni (NiO) (Fig. 3C) [24]. In Fig. 3D, only a very small peak was observed due to the low percentage of S and complex S species in NF/Ni-Mo-S. The presence of S may be verified in the XPS spectra for both Ni 2p and Mo 3d, indicating that S was successfully doped in Ni-Mo and may existed in several chemical states, including sulfide, metal sulfide and oxide [25-27].
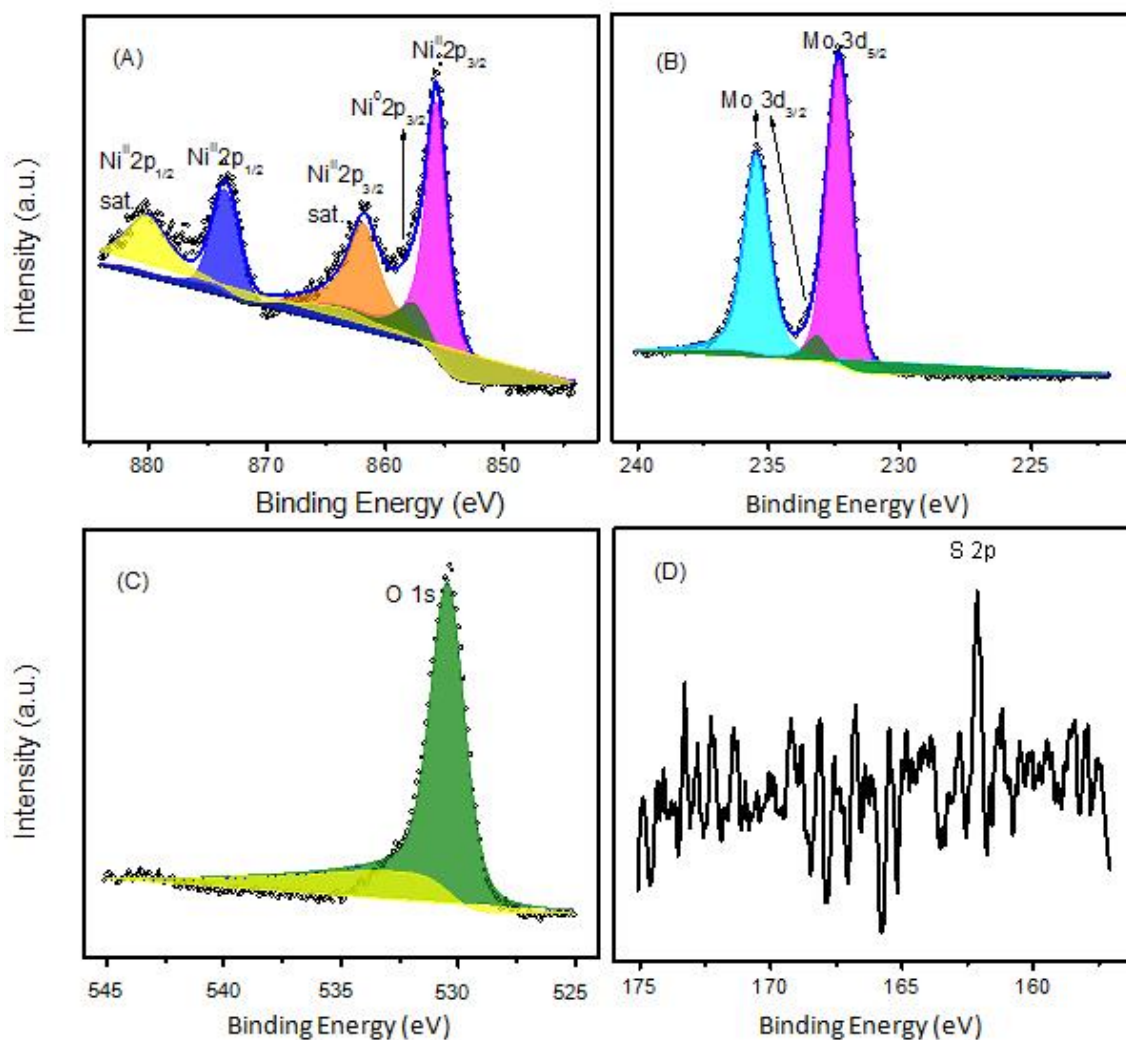
Figure 3. XPS spectra obtained for (A) Ni 2p, (B) Mo 3d, (C) O 1s and (D) S 2p in NF/Ni-Mo-S.

NF/Ni-Mo-S was predicted to exhibit better electrochemical performance than each of the constituent materials used in its preparation [28]. Fig. 4A-C shows the cyclic voltammograms (CVs) obtained for NF/Ni-Mo-S, NF/Ni-Mo-O' and NF/Ni-Mo-O at a scan rate of 0.1 V/s in 1M NaOH, which exhibit different abilities toward the glucose oxidation reaction. Obviously, both the current density

(193.2 mA/cm^2) and initiation potential (0.16 V) in the glucose oxidation reaction using NF/Ni-Mo-S was far better than those observed using NF/Ni-Mo-O or NF/Ni-Mo-O', indicating the glucose oxidation reaction was improved upon doping S into Ni-Mo-O during the high temperature calcination step. In Fig. 4C, the oxidation signal was not obvious due to the large background current of NF/Ni-Mo-O. It was found that high-temperature and S-doping play important roles toward enhancing the catalytic performance of NF/Ni-Mo-S. It was easy to conclude that NF/Ni-Mo-S displays a better loop area to be suitable as a supercapacitor [29]. Fig. 4D shows the CVs obtained for NF/Ni-Mo-S and NF recorded at a scan rate of 0.1 V/s in 1M NaOH with and without glucose. When compared with NF (curves c and d), after growing Ni-Mo-S on the surface of NF, a higher current density increase was observed in curves a and b, indicating that NF/Ni-Mo-S exhibits enhanced electrocatalytic performance toward glucose oxidation when compared to MF. To further investigate the electrocatalytic oxidation properties of NF/Ni-Mo-S toward glucose, the other two electrodes modified with Ni-Mo-O and NF were selected for comparison. The CVs of the three electrodes recorded in 1M NaOH containing 0.1 M glucose are shown in Fig. 4E. Clearly, NF/Ni-Mo-S exhibited the highest electrocatalytic oxidation activity and lowest onset over-potential among the three electrodes studied [30]. These results indicate that the introduction of S into Ni-Mo-O greatly improved its electrocatalytic properties.
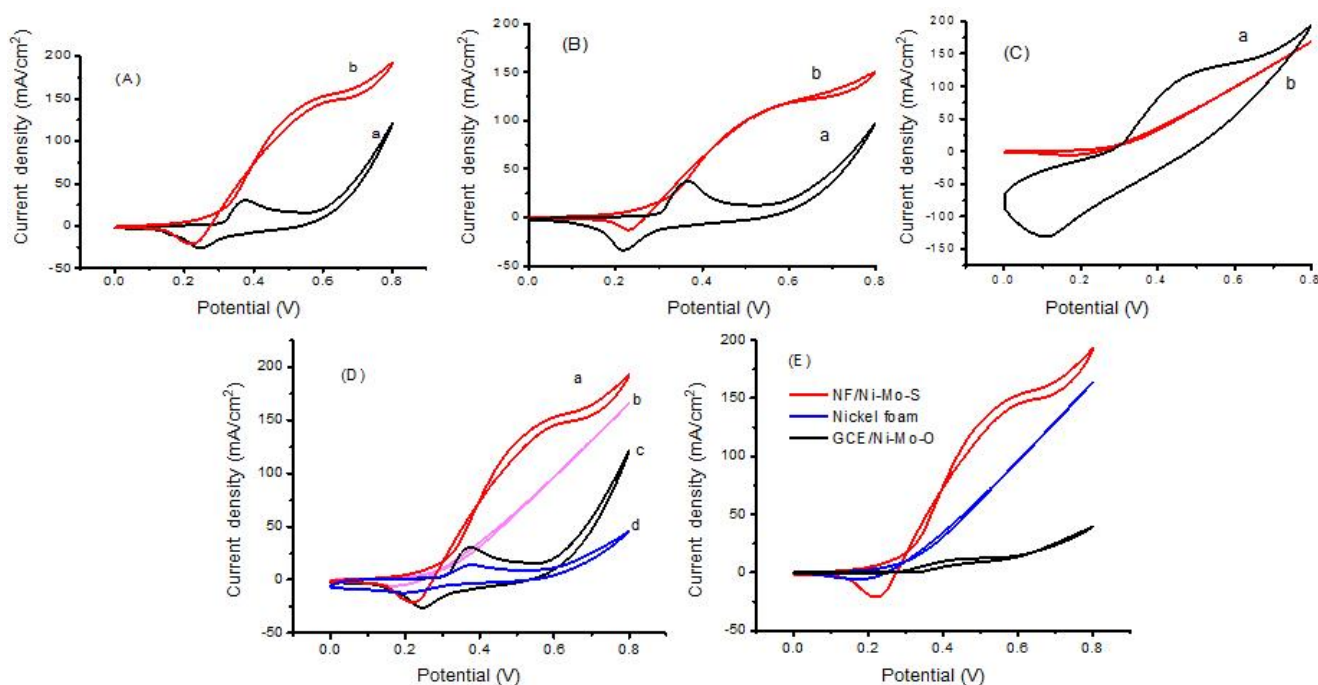
Figure 4. CVs recorded for (A) NF/Ni-Mo-S, (B) NF/Ni-Mo-O and (C) NF/Ni-Mo-O' in 1M NaOH with (b) and without (a) 0.1M glucose at a scan rate of 0.1 V/s. (D) CVs recorded for NF/Ni-Mo-S and NF in 1M NaOH (a, c) and without (b, d) with 0.1M glucose at a scan rate of 0.1 V/s. (E) CVs recorded for NF/Ni-Mo-S, Ni-Mo-O and NF in 1M NaOH containing 0.1M glucose at a scan rate of 0.1 V/s.

A Tafel slope, an inherent property of an electrocatalyst, was used to assess the electrocatalytic performance of NF/Ni-Mo-S, which was extracted from the linear portions of the corresponding Tafel

plots shown in Fig. 5A. Tafel plots describe the relationship between the overpotential and current density based on the following equation: $\eta = a + b\log(j)$, where a, b and j represent the dimensionless coefficient, Tafel slope and current density, respectively [31-32]. As seen, the Tafel slope of NF/Ni-Mo-S was 101 mV/dec and 174 mV/dec for the Pt/C. The smaller the Tafel slope, the faster the glucose oxidation rate increases. Therefore, NF/Ni-Mo-S displays enhanced electrocatalytic performance toward the oxidation of glucose when compared to Pt/C, and is superior to many recently reported metal sulfide catalysts [33].

　　　　The stability of NF/Ni-Mo-S was examined using galvanostatic measurements and the current-time test at 0.32 V in 1M NaOH containing 0.1 M glucose in a time period of 36000 s (Fig. 5B). The electrocatalytic signal of NF/Ni-Mo-S was relatively constant and no obvious decrease was observed before 27000 s. After 27000 s, the signal was slightly decreased and rapidly became stable, which was believed to be a transient state [34]. The *in situ* deposition or growth of the NF/Ni-Mo-S nanorod bundles and high temperature calcination step result in the close contact observed between the NF/Ni-Mo-S and electrode [35].
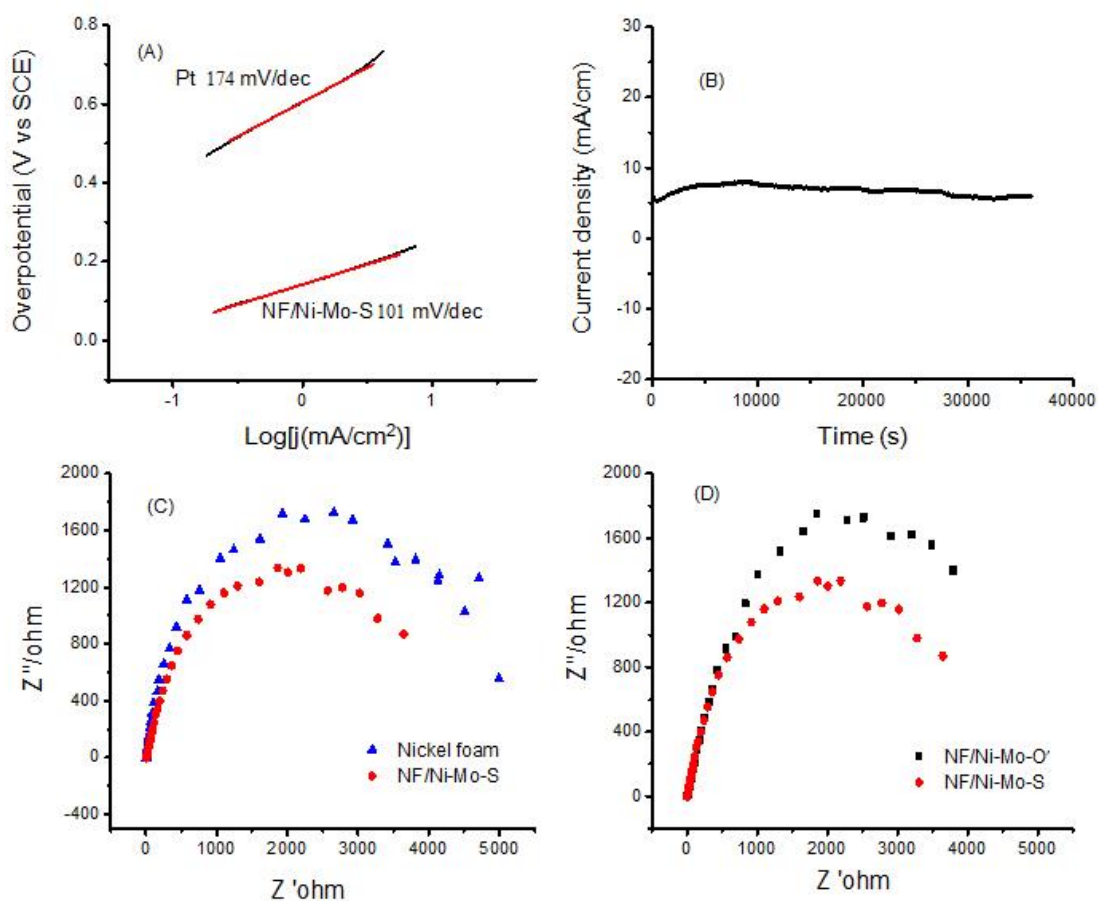
Figure 5. (A) Tafel plots obtained for the NF/Ni-Mo-S and Pt electrode in 1M NaOH containing 0.1M glucose. (B) The I-t curve obtained for NF/Ni-Mo-S under an overpotential of 0.32 V for 36000 s. EIS of (C) NF and NF/Ni-Mo-S, and (D) NF/Ni-Mo-O' and NF/Ni-Mo-S in 1M NaOH containing 0.1M glucose.

As an effective way to study the electrode surface properties and electrocatalytic performance, electrochemical impedance spectroscopy (EIS) is usually used to characterize electron transfer and diffusion [36]. Fig. 5C and D shows the representative Nyquist plots obtained for the electrodes modified using NF, NF/Ni-Mo-O' and NF/Ni-Mo-S, respectively. A semicircle was observed for each electrode, which was attributed to the electron transfer resistance. Obviously, NF/Ni-Mo-S displays a smaller semicircle than both NF and NF/Ni-Mo-O', showing the most efficient electron transportation, which may be a result of the high temperature calcination step under a sulfide-rich environment. In addition, all three electrodes do not show any obvious linear part in the low frequency region of their Nyquist plots. This means that the ions are rapidly diffused without any obvious diffusion impedance on the catalyst surface [37-39].

The anodic and cathodic peaks originate from the Faradaic redox reactions of the Ni cations, which mainly govern the capacitance characteristics [40-42]. Fig. 6A shows the CV curve obtained for NF/Ni-Mo-O; both the current density and encircled area are much larger when compared to NF, indicating the higher specific capacitance of NF/Ni-Mo-O. This means that the capacitance can be increased by the *in-situ* growth of cluttered nanorods of Ni-Mo-O within NF. Fig. 6B shows that the capacitance becomes larger when the scan rate is increased because the mass transfer resistance and polarization increased in the electrochemical processes necessary for pseudocapacitive performance. The specific capacitance C (F/g) were assessed using the following equation [43]:

$$C = \frac{\int_{V_2}^{V_1} I\, dV}{v(V_2 - V_1)m}$$

where $\int_{V_2}^{V_1} I\, dV$, v, V_1 and V_2 refer to the area of CV curve in discharge process, potential scan rate (V/s), final potential (V) and initial potential (V), respectively, and m represents the mass of the materials. Fig. 6C shows the change in the specific capacitance observed for NF/Ni-Mo-O at different scan rates, where the specific capacitances were 2074.8, 1292.5, 884.35, 418.4 and 244.9 F/g at scan rates of 5, 10, 20, 50 and 100 mV/s, respectively. The specific capacitance gradually decreased upon the increasing scan rate as a result of the slow redox reaction observed at higher rates [44]. The Ni-Mo-O nanorod bundles possessed adequate gaps (Fig. 1) to transport OH^- ions into the electrolyte solution and thus, have a high specific surface area, excellent exposure to ions, highly efficient diffusion and strong ability to store OH^- ions [45]. In addition, the cycling stability of NF/Ni-Mo-O was measured and calculated (Fig. 6D). A scan rate of 100 mV/s was applied to measure the change in the specific capacitance with time. The specific capacitance values of NF/Ni-Mo-O were 232.4 and 203.8 F/g. at the 1st and 2000th cycles, respectively. Importantly, the specific capacitance after 2000 cycles was maintained at 87.7% of its initial value, indicating its excellent stability as a result of the strong attachment between Ni-Mo-O and NF.
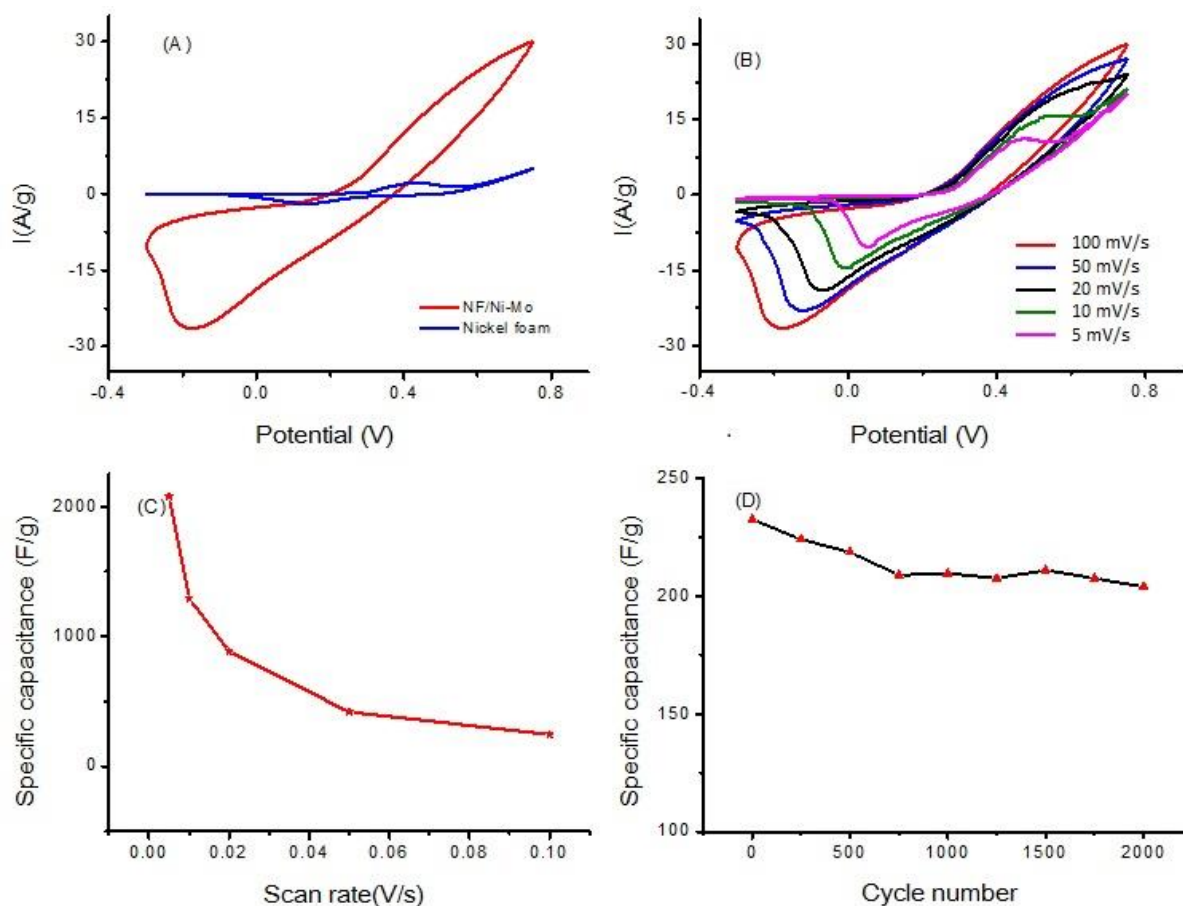
Figure 6. CVs recorded for (A) NF/Ni-Mo-O and NF at a scan rate of 100 mV/s and (B) NF/Ni-Mo-O at scan rates from 5 to 100 mV/s in 1M NaOH. (C) The specific capacitance of NF/Ni-Mo-O observed at different scan rates. (D) The long-term cycle stability of NF/Ni-Mo-O observed at a scan rate of 100 mV/s.

4. CONCLUSIONS

Ni-Mo-O nanorod bundles were calcined at a high temperature (500 °C) under a sulfur atmosphere to prepare NF/Ni-Mo-S. NF/Ni-Mo-S has a high specific surface area due to the radial growth of Ni-Mo-S nanorod bundles inside NF, which has a highly porous structure and large specific surface area. When compared with other catalysts, NF/Ni-Mo-S exhibited good electrocatalytic performance toward the oxidation of glucose at a low onset potential. Moreover, this work provides a simple, efficient and environmentally friendly method of preparing NF/Ni-Mo-O as a pseudocapacitor, which exhibited comparable electrochemical capacitance performance and outstanding stability.

References

1. S.B. Aoun, G.S. Bang, T. Koga, Y. Nonaka, T. Sotomura and I. Taniguchi, *Electrochem. Commun.,* 5(2003)317.
2. D.V. Pham, R.A. Patil, C. Yang, W. Yeh, Y. Liou and Y. Ma, *Nano Energy,* 47(2018)105.
3. K. Elouarzaki, A. Le Goff, M. Holzinger, J. Thery and S. Cosnier, *J. Am. Chem. Soc.,* 134(2012)14078.
4. S.H. Liao, S.Y. Lu, S.J. Bao, Y.N. Yu and M.Q. Wang, *Anal. Chim. Acta,* 905(2016)72.
5. B. Jin, G. Yao, X. Wang, K. Ding and F. Jin, *ACS Sustain. Chem. Eng.,* 5(2017)6377.
6. Y. Miao, J. Wu, S. Zhou, Z. Yang and R. Ouyang, *J. Electrochem. Soc.,* 160(2013)B47.
7. X. Xiao, S. Peng, C. Wang, D. Cheng, N. Li, Y. Dong, Q. Li, D. Wei, P. Liu, Z. Xie, D. Qu and X. Li, *J. Electroanal. Chem.,* 841(2019)94.
8. Y. Ji, J. Liu, X. Liu, M.M.F. Yuen, X.-Z. Fu, Y. Yang, R. Sun and C.-P. Wong, *Electrochim. Acta,* 248(2017)299.
9. T.Q.N. Tran, S.W. Yoon, B.J. Park and H.H. Yoon, *J. Electroanal. Chem.,* 818(2018)76.
10. K. Zhou, Y. Zhu, X. Yang and C. Li, *Electroanal.,* 22(2010)259.
11. M. Zhou, R. Ouyang, Y. Li and Y. Miao, *Electrochim. Acta,* 246(2017)9.
12. F. Luan, S. Zhang, D. Chen, F. Wei and X. Zhuang, *Microchem. J.,* 143(2018)450.
13. R. Madhuvilakku, R. Mariappan, S. Jeyapal, S. Sundar and S. Piraman, *Ind. Eng. Chem. Res.,* 52(2013)17407.
14. W. Wu, B. Yu, H. Wu, S. Wang, Q. Xia and Y. Ding, *Mat. Sci. Eng. C-Mater.,* 70(2017)430.
15. S. Wang, S. Zhang, M. Liu, H. Song, J. Gao and Y. Qian, *Sensor. Actuat. B-Chem.,* 254(2018)1101.
16. D. Fa, M. Zhou, H. Zhao, Y. Jiang and Y. Miao, *Polyhedron,* 144(2018)11.
17. M. Zhou, Y. Liu, D. Fa, L. Qian and Y. Miao, *Electrochim. Acta.,* 259(2018)329.
18. L. Tan, W. Wu, Q. Yin, X. Ke, R. Qiao, G. Tong and L. Zhu, *J. Ind. Eng. Chem.,* 52(2017)349.
19. Z.-Y. Yu, C.-C. Lang, M.-R. Gao, Y. Chen, Q.-Q. Fu, Y. Duan and S.-H. Yu, *Energ. Environ. Sci.,* 11(2018)1890.
20. D. Wei, Y. Zhang, X. Zhu, M. Fan and Y. Wang, *J. Alloy. Compd.,* 824(2020)153937
21. J. Balamurugan, C. Li, V. Aravindan, N.H. Kim and J.H. Lee, *Adv. Funct. Mater.,* 28(2018)1803287.
22. J. Balamurugan, S.G. Peera, M. Guo, T.T. Nguyen, N.H. Kim and J.H. Lee, *J. Mater. Chem. A,* 5(2017)17896.
23. Y. Wang, W. Sun, X. Ling, X. Shi, L. Li, Y. Deng, C. An and X. Han, *Chem-Eur. J.,* 26(2019)4097.
24. C. Zhang, Y. Zhang, S. Zhou and C. Li, *J. Alloy. Compd.,* 818(2020)152833.
25. N.J. Hartmann, G. Wu and T.W. Hayton, *J. Am. Chem. Soc.,* 138(2016)12352.
26. A. Irshad and N. Munichandraiah, *ACS Appl. Mater. Inter.,* 9(2017)19746.
27. F. Soyekwo, Q. Zhang, R. Gao, Y. Qu, R. Lv, M. Chen, A. Zhu and Q. Liu, *J. Mater. Chem. A,* 5(2017)583.
28. J. Li, Y. Peng, W. Zhang, X. Shi, M. Chen, P. Wang, X. Zhang, H. Fu, X. Lv, F. Dong and G. Jiang, *Appl. Surf. Sci.,* 509(2020)145369.
29. R. Asadi, A.M. Zardkhoshoui, S.N. Azizi and S.S. Hosseiny Davarani, *ChemElectroChem,* 6(2019)5984.
30. Z. Liu, C. Pan, W. Li, S. Wei, M. Zhang and S. Chen, *Electrochim. Acta.,* 338(2020)135897.
31. Z. Ma, H. Meng, M. Wang, B. Tang, J. Li and X. Wang, *ChemElectroChem,* 5(2018)335.
32. M. Xiao, Y. Miao, W. Li, Y. Yang and X. Liang, *Electrochim. Acta.,* 178(2015)209.
33. Q. Guo, T. Wu, L. Liu, Y. He, D. Liu and T. You, *J. Alloy. Compd.,* 819(2020)153376.
34. S. Zhang, X. Zhang, J. Li and E. Wang, *J. Mater. Chem. A,* 5(2017)20588.
35. Z. Han, X. Liang, S. Wang, L. Zhou and Z. Zhao, *Mater. Lett.,* 246(2019)63.
36. F. Dong, X. Liu, M. Irfan, L. Yang, S. Li, J. Ding, Y. Li, I.U. Khan and P. Zhang, *Int. J. Hydrogen Energ.,* 44(2019)8178.
37. H. Li, Y. Zhang, Q. Wan, Y. Li and N. Yang, *Carbon,* 131(2018)111.

38. Y. Tian, M. Zhou, X. Meng, Y. Miao and D. Zhang, *Mater. Chem. Phys.,* 198(2017)258.
39. M. Xiao, D. Yang, Y. Yan, Y. Tian, M. Zhou, M. Hao, R. Cheng and Y. Miao, *Electrochim. Acta.,* 180(2015)260.
40. K. Chen, Y. Yang, K. Li, Z. Ma, Y. Zhou and D. Xue, *ACS Sustain. Chem. Eng.,* 2(2014)440.
41. P. Zhang, Y. Yang, Z. Ma, Y. Wang, Y. Pan and C. Lu, *Mater. Lett.,* 164(2016)421.
42. C. Hsieh, C. Huang, Y. Chen and S. Lu, *Appl. Catal. B-Environ.,* 267(2020)118376.
43. W. Hu, L. Chen, M. Du, Y. Song, Z. Wu and Q. Zheng, *Electrochim. Acta.,* 338(2020)135869.
44. X. Xu, J. Shen, N. Li and M. Ye, *J. Alloy. Compd.,* 616(2014)58.
45. H. Xuan, T. Liang, G. Zhang, Y. Guan, H. Li, R. Wang, P. Han and Y. Wu, *J. Alloy. Compd.,* 818(2020)153350.